Chem

CellPress
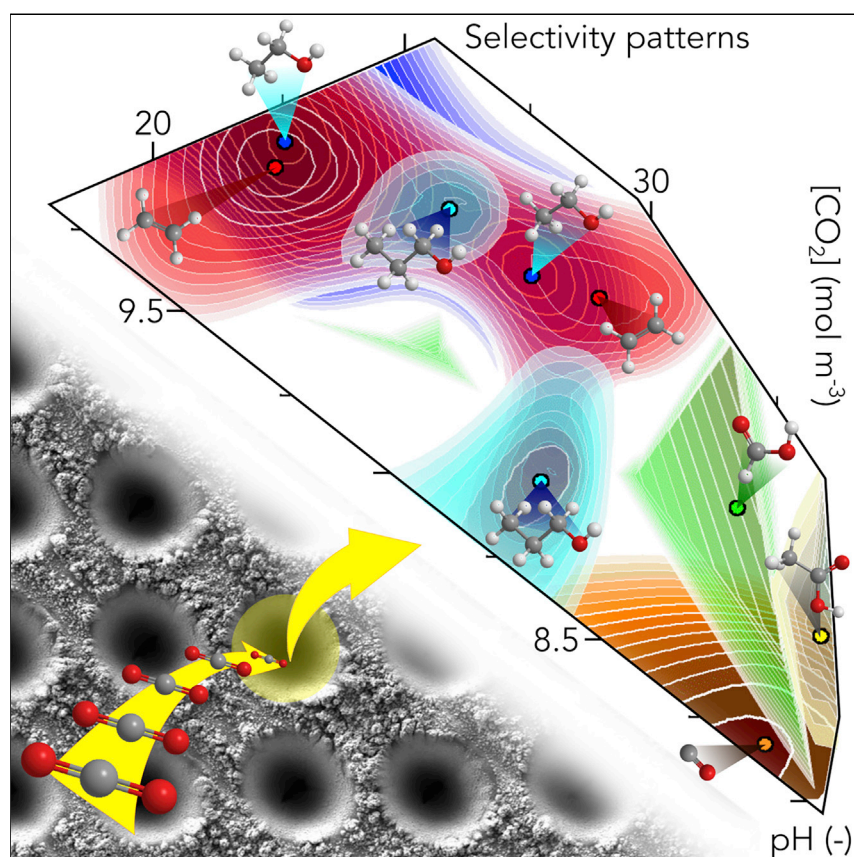
Article

Laser-Microstructured Copper Reveals Selectivity Patterns in the Electrocatalytic Reduction of CO_2

Florentine L.P. Veenstra,
Norbert Ackerl, Antonio J.
Martín, Javier Pérez-Ramírez

jpr@chem.ethz.ch

HIGHLIGHTS

Selectivity in the CO_2 electroreduction has been mapped against the chemical environment

Maps provide mechanistic insights for unexplored routes such as propanol formation

Maps can predict the effect of operating parameters such as electrolyte or stirring

The local (electro)chemical environment largely influences the selectivity toward, for example, olefins or alcohols in the electroreduction of CO_2 over copper (Cu)-based catalysts. However, this factor is mostly qualitatively understood. Here, by combining catalytic results from a set of laser-microstructured Cu electrodes with defined geometries and accurate modeling including bulk and local effects, we map the effect of local pH and CO_2 concentration for the main products. We also show how our results are useful for device engineering.

Chem

CellPress

Article

Laser-Microstructured Copper Reveals Selectivity Patterns in the Electrocatalytic Reduction of CO$_2$

Florentine L.P. Veenstra,[1] Norbert Ackerl,[2] Antonio J. Martín,[1] and Javier Pérez-Ramírez[1,3,*]

SUMMARY

The strategy of engineering the local chemical environment to direct selectivity in the electroreduction of CO$_2$ toward value-added products is only qualitatively understood. The unfeasibility of local concentration measurements and the limited applicability of simulations to practical systems hinder more precise guidelines. Here, we quantify the impact of the (electro)chemical environment on the selectivity pattern by using microstructured copper (Cu) electrodes prepared by ultra-short pulse laser ablation. We created regularly distributed micro-probes and assessed their product distributions at distinct overpotentials. The regular geometry enabled the accurate simulation of the local pH and CO$_2$ concentration. Selectivity maps useful for mechanistic and applied studies emerged. They revealed clear patterns for C$_1$–C$_3$ products, suggesting novel insights, such as the presence of two reaction mechanisms for propanol. The effect on the selectivity pattern of operating parameters, such as enhanced mass transport and electrolyte composition, was also predicted by the maps.

INTRODUCTION

The electrocatalytic CO$_2$ reduction reaction (eCO$_2$RR) toward fuels and chemicals in aqueous media must still overcome technological challenges to contribute toward a sustainable, circular economy. The lack of selectivity control on copper (Cu)-based systems stands out among them given that Cu is the only material known to promote value-added products, such as hydrocarbons, alcohols, and aldehydes, at appreciable rates.[1–3] The insufficient understanding of the variables to be optimized hinders precise strategies for catalyst design, operating conditions, and electrode engineering.[4,5]

Historically, research in this field has been focused on materials development,[6,7] but the recent recognition of the local (electro)chemical environment as a key directing agent for selectivity has opened new avenues. The applied potential and the surface coverage of H and CO$_2$ are central parameters influencing the eCO$_2$RR and the competing hydrogen evolution reaction (HER). However, their separated analysis is unattainable because they are intertwined in the double-layer region by the carbonate chemical equilibria, the diffusion processes, and the interaction of charged species in the intense electric field.[4] Despite the complexity involved, the literature shows how activity and/or selectivity can be successfully enhanced via locally tuned electric fields,[8] highly alkaline environments,[9,10] mixed chemical-electrocatalytic reduction routes,[11] or free cationic and anionic species present.[12,13] In this context, rationalization efforts have become necessary for translating these observations into quantitative guidelines for the optimization of the local environment. These efforts

The Bigger Picture

It is of utmost importance to convert CO$_2$ into useful compounds to close the carbon cycle. Through electroreduction, value-added compounds can be obtained when using a copper (Cu)-based catalyst, albeit with limited control on the product distribution. Currently, we know qualitatively that the latter is largely influenced by the environment next to the electrode surface, but a deeper understanding of this effect is necessary for transforming it into an effective design tool for material and process optimization.

By combining experiments and simulations on laser-microstructured Cu electrodes with defined geometries, we quantified the effect of the (electro)chemical environment on the product distribution, generating selectivity maps that accurately predict the influence of key operating conditions. Our study thus provides a powerful tool for engineering devices for the distributed production of fuels and chemicals as it is of direct application in the so-called artificial leaves.

ɚ CellPress

Chem
Article

are currently focused on C_1 and C_2 products,[4,14–16] and there are virtually no indications for more complex ones.

Ethylene formation is a prominent example. The fact that its selectivity can be improved in a practical gas diffusion electrode from 30% to ca. 70% upon optimization of mass transport and electrolyte pH clearly reflects the sensitivity of this reaction to the environment.[9] In this regard, theoretical works predict the pH sensitivity of the rate-determining step in C–C coupling to be due to a non-simultaneous proton-electron transfer.[17] This idea has led to diverse proposed mechanisms toward ethylene formation at different overpotentials with varying pH sensitivity[17,18] and its promotion by high local CO_2 concentration through enhanced CO coverage.[19] Neither the precise route(s) nor a quantitative description of the local environments under which they are promoted has been firmly established. Remarkably, ethanol is thought to share a significant portion of its reaction pathway with ethylene and therefore some of these features.[14,20,21] In parallel, local conditions may also affect the parasitic HER, for which high activity has been associated with enhanced mass transport properties.[22] Unfortunately, the relevance of quantifying the local electrochemical environment is in stark contrast with the ability to measure or model the concentrations of species in the vicinity of the electrode. This fact originates from the technical limitations of the operando techniques[23] and the usually complex morphology of the catalysts in the relevant micrometer scale, which provides results from forcibly simplistic models, mostly with a qualitative value.[24,25] The lack of well-structured systems has not allowed a systematic study of mass transport, chemical equilibria, and local cationic buffer effects.[26] With this in mind, Cu-based surfaces with a variable degree of control have been reported, as in the case of foams[27,28] or mesostructured layers with variable thickness.[29] They have confirmed with limited quantification, for example, the improved selectivity toward C_2 products under severe mass transport limitations. A clever templating strategy experimentally linked cylindrical nanoporosity and larger rates of C_2 products rationalized through local concentration gradients and confinement effects.[30] Nonetheless, selectivity could not be linked to intrinsic physicochemical parameters but rather to the length of nanocavities.

Microfabrication can contribute to this need to describe selectivity patterns in terms of chemical environment descriptors by providing catalysts with controlled geometry. This set of techniques has been demonstrated through lithographic approaches to gather insights into the formation and nature of active sites in multicomponent systems[31,32] and into the operation of bifunctional catalysts.[33] In this study, we identified ultra-short pulsed (USP; pulse duration from femtoseconds to picoseconds) laser ablation[34,35] as the technique of choice for the development of model Cu electrodes. Whereas nanosecond pulsed laser ablation is a well-established technique for nanoparticle synthesis,[36] USP laser ablation has only found application in the field of catalysis to enhance electrode roughness.[37] Its sub-micrometer resolution (mostly limited by diffraction) displays great potential for precise structuring as a result of the small energy input per pulse that creates negligible heat-affected zones.[38] This feature adds to rapid processing[39] (up to 1 m^2 min^{-1}) and the ability to alter the chemical nature of the ablated surface when applied under reactive atmospheres.[40,41] We ablated Cu foils by using this platform to develop microstructured CuO electrodes amenable to product quantification. We designed them as a dense, regular distribution of conical cavities (denoted as micro-probes) spanning a wide range of lengths.

The combination of applied potentials and micro-probe lengths imposed distinct local electrochemical environments due to the concentration gradients arising from the electrochemical reactions, CO_2 and cation hydrolysis equilibria, and

[1]Institute for Chemical and Bioengineering, Department of Chemistry and Applied Biosciences, ETH Zürich, 8093 Zürich, Switzerland

[2]Institute for Machine Tools and Manufacturing, Department of Mechanical and Process Engineering, ETH Zürich, 8005 Zürich, Switzerland

[3]Lead Contact

*Correspondence: jpr@chem.ethz.ch

https://doi.org/10.1016/j.chempr.2020.04.001

Chem
Article

CellPress

geometry. These environments could be quantitatively described after three-dimensional (3D) simulations, which enabled the emergence of selectivity patterns in the form of maps for a variety of C_1–C_3 products expressed in terms of local CO_2 concentration and pH. Selectivity maps emerge as valuable resources for theoretical studies and as guiding tools toward optimized operating parameters.

RESULTS AND DISCUSSION

This section initially describes the preparation and characterization of microstructured Cu electrodes and the associated selectivity patterns at different potentials. This set of results is subsequently used as input for 3D models, enabling the quantification of the local chemical environment under eCO$_2$RR conditions. As a result, selectivity patterns for C_1–C_3 products emerge with the simulated local pH and CO_2 concentration as descriptors. Finally, a mechanistic discussion and an analysis of the influence of operating parameters based on obtained maps close the section.

Fabrication and Characterization of Microstructured Electrodes

The driving idea of this study is to enable the imposition of different local chemical environments under operating conditions while keeping both the potential and the catalyst unaltered. To this end, we aimed to design model electrodes whose geometry could influence mass transport properties and thus the local concentrations of species. Inspired by monoliths widely applied in thermocatalytic processes,[42] we anticipated that the mean diffusion pathway between the active walls and the external environment would be controlled in a cylindrical or conical micro-reactor by its length. The fabrication of their analogs in a Cu foil demanded the ability to create regular cavities at the relevant micrometer scale in a practical catalytic layer in a gas diffusion electrode.[43] On this basis, we applied USP laser ablation to transform Cu foils into model electrodes, as shown in Figure 1. The ablation was performed in air, given the enhanced production of complex products generally observed over oxidic Cu surfaces.[3]

In more detail, a first ablation step pretreated the foils by removing ca. 2 µm of material to produce a submicrometrically roughened surface called LA-Cu-0 (where 0 denotes zero; Figures 1A and S1), whose composition was identified as CuO after X-ray diffraction (XRD) and X-ray photoelectron spectroscopy (XPS) analyses (Figures 1B, 1C, and S2, respectively). Importantly, to understand the effect on the catalytic performance introduced by the USP laser ablation treatment, we first compared selectivity patterns under CO_2-saturated 0.1 M KHCO$_3$ (pH 6.8) for the unprocessed Cu foils and LA-Cu-0 surface (Figure 2).

The results show that the application of laser ablation brings a modest influence for carbon monoxide, formate, and ethylene (Figure 2A) but enhances the formation of alcohols and suppresses the formation of acetate (Figure 2B). The post-reaction characterization of LA-Cu-0 confirmed the expected reduction of CuO into Cu (Figures 1B, 1C, and S2). In this regard, improved rates toward ethylene and/or alcohols on oxide-derived Cu have been repeatedly reported (though not in all cases[44,45]), but their origin is subject to a vivid debate.[3] Modified selectivity has been linked to the formation upon reduction of the oxide of particular active sites, such as grain boundaries,[46,47] remaining interstitial oxygen,[48] or low-coordinated Cu sites.[49] Nonetheless, the idea of the chemical environment primarily directing the selectivity over these materials due to their unusually large roughness (provoking strong local pH and CO_2 concentration gradients) has been gaining relevance and is now openly
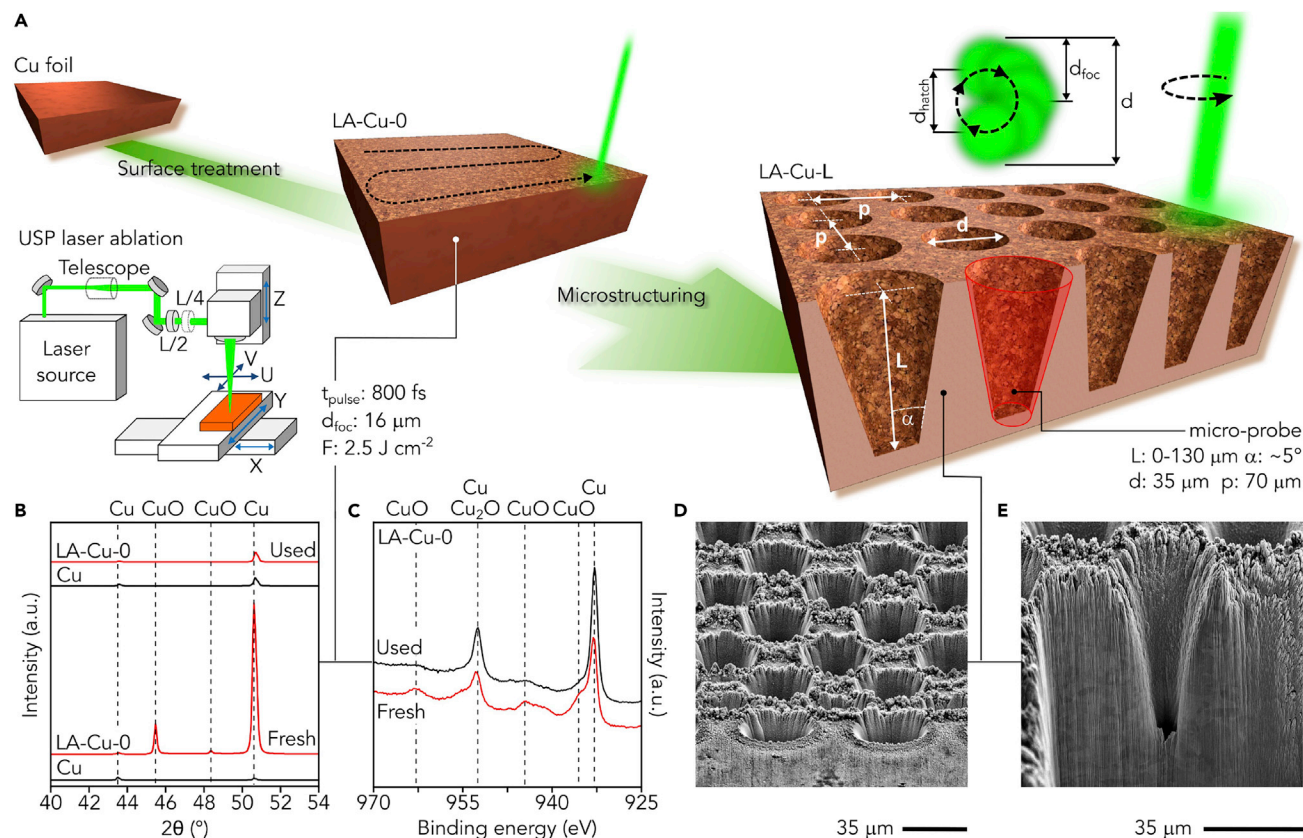
Figure 1. Microfabrication and Basic Characterization of Microstructured Electrodes

(A) The USP laser beam was guided from the source in open space to a galvo scanner through modifying optics, resulting in a focal diameter (d_{foc}). Kinematic (XYZ) and optical (UV) axes allowed precise alignment of the laser and the Cu substrate, whereas galvo mirrors enabled fast circular hatching (d_{hatch}) and distribution of the laser pulses for material removal. Cu foils were initially pretreated by ablation of a 2 μm layer (LA-Cu-0) and subsequently patterned to create regular arrays of micro-probes with different lengths (LA-Cu-L).

(B) XRD patterns before (Cu) and after (LA-Cu-0) laser ablation.

(C) XPS spectra of LA-Cu-0 before and after electrolysis.

(D) Micrograph showing the periodically aligned micro-probes and a partially removed surface layer.

(E) Representative PFIB-SEM cross-sectional micrograph of one micro-probe. Case shown: LA-Cu-100 after exposure to reaction conditions.

claimed.[3,30,50] In accordance, we notice that the catalytic performances in our case differ mainly at high potentials (i.e., larger currents) and that ablation increased the roughness by a factor of 3 (Table S1) as a result of redeposition of Cu as debris (Figure S1).

We subsequently microstructured the laser-ablated LA-Cu-0 surface to obtain the set of model electrodes. A dense regular distribution of conical micro-probes (Figure S3) was prepared by a circular hatch of the laser beam (see Figure 1A and the Supplemental Experimental Procedures for a full description). We kept their diameter and pitch constant (Figures 1D and 1E), whereas their length was controlled by the number of incident laser pulses. The resulting electrodes (2.25 cm²) contained ca. 92 000 micro-probes and are denoted according to their length (LA-Cu-L, where L = 0, 20, 40, 60, 100, or 130 μm). This strategy achieved a quasi-linear dependency of the exposed surface area with L in spite of some deviations from the conical shape due to reflections of the laser beam, as disclosed by microcomputed tomography (Figure S4). With regard to their chemical nature, all LA-Cu-L electrodes showed similar composition (Figure S5), confirming the feasibility of this approach toward

Chem
Article
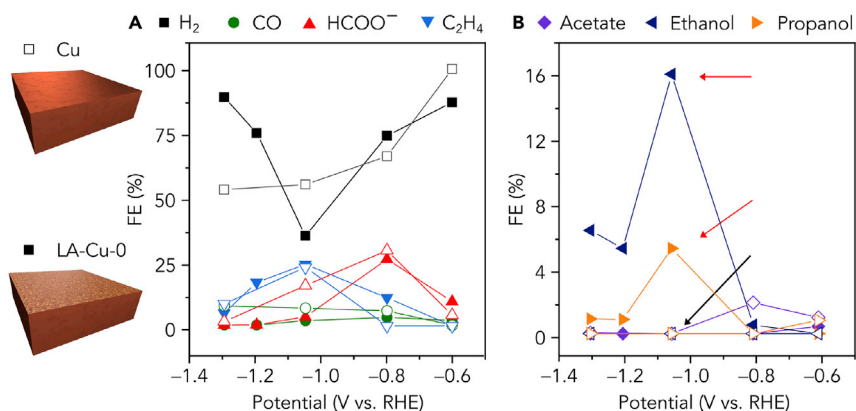
Figure 2. FE versus Potential for a Cu Foil before (Cu, Void Symbols) and after (LA-Cu-0, Filled Symbols) Laser Ablation

Products where Cu and LA-Cu-0 show qualitatively similar trends (A) and products where LA-Cu-0 outperforms Cu (B) are highlighted for the case of propanol and ethanol (black arrow, Cu; red arrows, LA-Cu-0). Products detected at trace levels are not included (see Table S2).

a set of chemically identical microstructured electrodes with favorable catalytic performance, enabling the study of a variety of products.

Revealing Selectivity Patterns by Varying Applied Potential and Electrode Geometry

Qualitatively, we expected larger L and more negative potentials to increase the average local pH and reduce the concentration of CO_2. Following this reasoning, we evaluated the performance of the microstructured electrodes at different potentials (V = −0.6, −0.8, −1.05, and −1.3 V versus reversible hydrogen electrode [RHE]) as described in the Supplemental Experimental Procedures. Exposure to reaction conditions did not alter the structure of these electrodes, as revealed by scanning electron microscopy (SEM) (Figure S6). Cyclic voltammetries did not show unexpected redox signals or degradation either (Figure S7). We carefully quantified products with modest faradic efficiencies (FEs) in view of their value to discuss potential mechanistic routes (see Figure S8 and Table S2). The set of major products was common across all conditions (Figure 2 and Table S3).

Selectivity patterns are presented as maps in Figure 3 for representative C_1 (formate), C_2 (ethanol), and C_3 (propanol) products and for the rest in Figure S9. Variations in selectivity at a fixed potential must be ascribed to the different geometry of the electrodes. A quick inspection reveals the predominance of C_1 products at low potentials and of C_2 at larger ones (Figure S9), as reported earlier over non-structured Cu,[51] with minor impact of L. Turning into particular products, formate (Figure 3) was produced with relatively high selectivity (30%–40%) over a wide zone at all L values with no clearly discernible pattern. In contrast, CO was formed with no exception at low quantities (Figure S9 and Table S3), as was the case for oxide-derived Cu catalysts with mild roughness promoting complex products.[50] More interestingly, the maps for ethylene (Figure 3) and ethanol (Figure S9) resemble each other considerably, suggesting partially shared mechanistic routes as already proposed by theoretical studies.[4] Figure S10 provides the corresponding maps for ethanol and ethylene versus the standard hydrogen electrode (SHE) to account for the claimed pH dependency of the proposed rate-determining C–C coupling step.[17] Finally, propanol (Figure 3) is favored (6%–7% FE) over two different regions partly overlapping the C_2 products, thus suggesting similarities among mechanisms.[52,53]
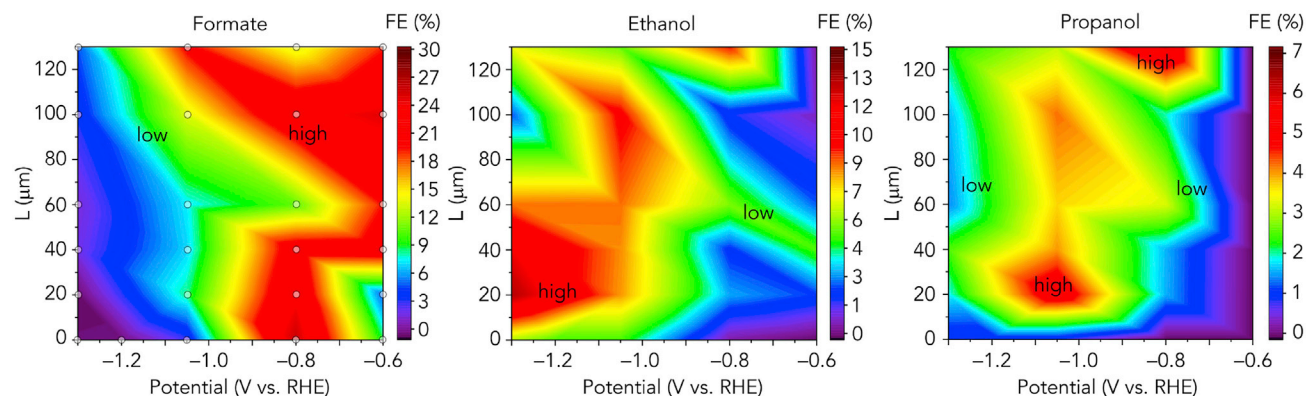
Figure 3. Selectivity Maps versus Applied Potential and Geometry on Microstructured Electrodes
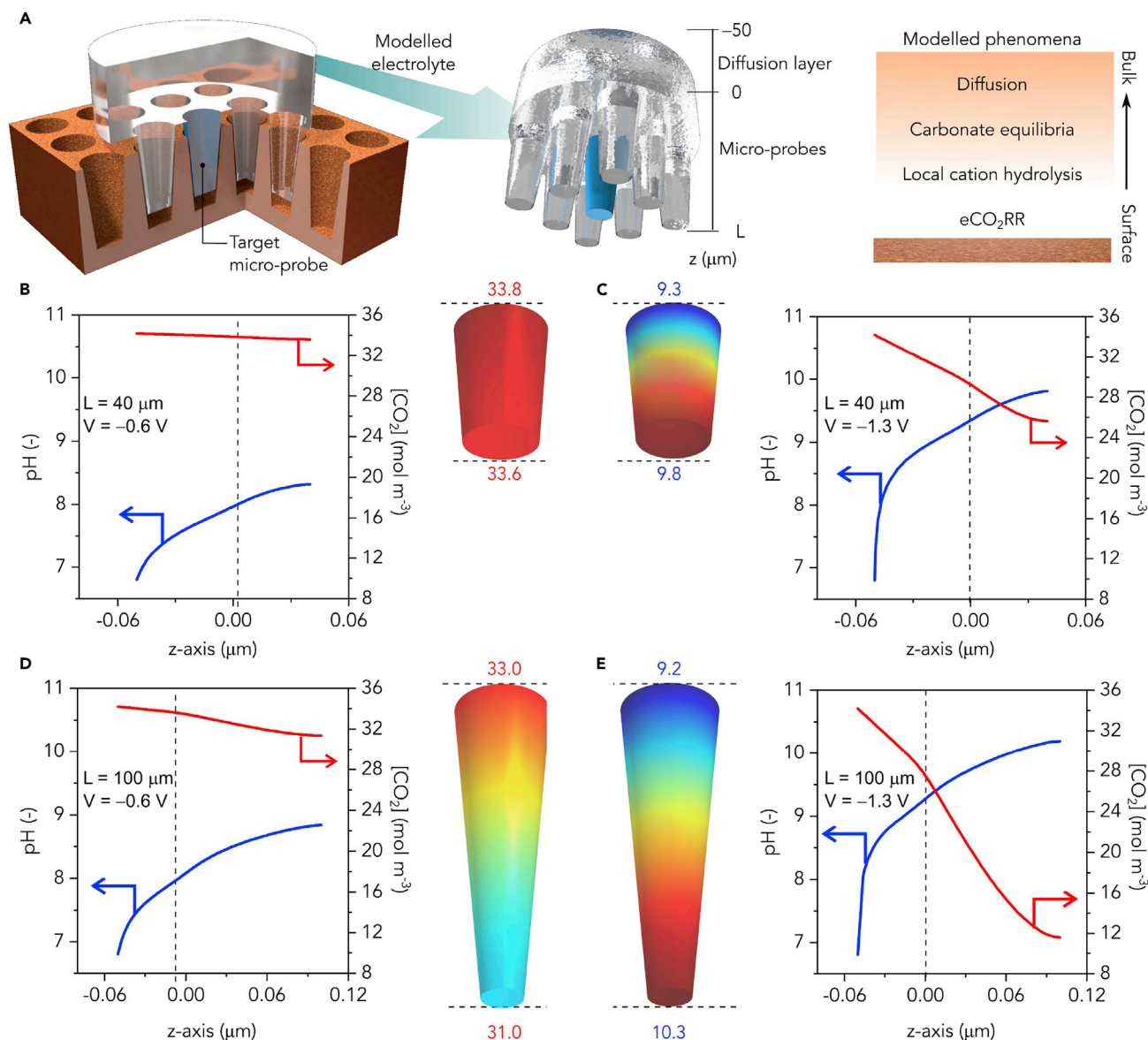
Contour maps showing FE for representative C_1 (formate), C_2 (ethanol), and C_3 (propanol) products versus micro-probe length (L) and potential. They were built upon integration of results obtained for L = 0, 20, 40, 60, 80, 100, and 130 μm measured at −0.6, −0.8, −1.05, and −1.3 V versus RHE, as indicated by gray dots in the formate map. All other products are depicted in Figure S9. The performance of non-structured laser ablated regions among micro-probes was assimilated to that of Cu-LA-0 (see the Supplemental Experimental Procedures for details).

Even though these results establish the feasibility of varying the geometry of the electrodes to obtain selectivity patterns, these maps show very limited practical relevance at this stage given that they reflect the performance of this particular set of electrodes under certain operating conditions. We thus aimed to obtain selectivity maps of more general applicability by translating potential and L into average local pH and CO_2 concentration in the interior of the micro-probes.

Modeling the Local Chemical Environment under Operating Conditions on Microstructured Electrodes

The required quantitative description of the local chemical environment was attained by computational modeling. The set of experimental results comprising current densities (Table S4) and FEs (Tables S2 and S3) alongside the geometry of the electrodes were used as input for 3D simulations targeting the concentrations and fluxes of relevant species on the flat surface and within the interior of the micro-probes. Most of the assumptions contained in our model are comparable to those found in other works developed over more ill-defined[24] or flat[54] surfaces (Tables S5–S7). We nonetheless remark that the model considers the local buffer effect of hydrolysis of cations (Table S8) as proposed by Singh et al.[12] The Supplemental Experimental Procedures provide a detailed description of the model.

The modeled electrolyte included three regions (Figure 4A). The first one encompasses the volume contained in the micro-probe under analysis as defined in Figures 1 and S4. To include the potential effect of neighboring micro-probes, we added the eight adjacent micro-probes as the second region. The third region accounts for the diffusion layer, as it was considered the dominant mass transport mechanism at this scale. Its thickness accounts for the degree of convection and can be tuned to simulate enhanced (small thickness) or impeded (large thickness) mass transport in the bulk of the solution. Its value (50 μm) reflects the mild convection imposed in the cathodic chamber by CO_2 bubbling (see the Supplemental Experimental Procedures for a more extended description). The concentration and flux of OH^-, CO_2, HCO_3^-, and CO_3^{2-} species were calculated at steady state upon considering the interplay between the eCO2RR and HER activities (Table S4), the chemical equilibria of carbonate species (Table S6), the local buffer effect of the hydrolysis of cations, and diffusion (Table S7).
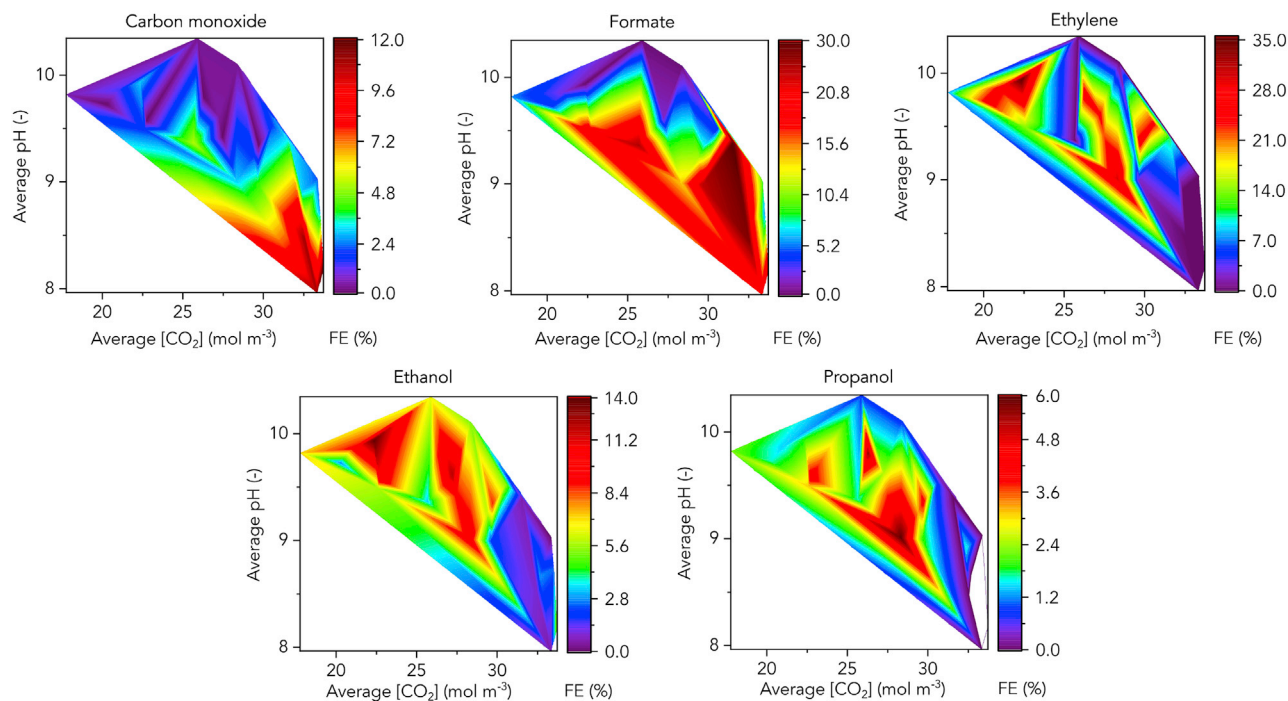
Chem
Article

CellPress

Figure 4. Computational Modeling under eCO2RR Conditions

(A) The concentrations of relevant species in the interior of the micro-probe under analysis (blue) were calculated upon modeling according to a finite-element approach in the COMSOL platform. The modeled electrolyte also comprised the interior of the eight adjacent micro-probes and the diffusion layer. Modeled phenomena are indicated.

(B–E) Calculated evolution of pH and CO_2 concentration along the longitudinal axis (z axis) for selected lengths and potentials. The z coordinate increases toward the interior and is zero at the base of the micro-probe. Insets show the three-dimensional representation of the simulated CO_2 concentration (at −0.6 V versus RHE) or pH (at −1.3 V versus RHE).

As boundary conditions, we imposed bulk concentrations at the free end of the diffusion layer (z = −50 μm in Figure 4A), zero flux for non-reactive species on the Cu surfaces, zero flux for all species on the lateral walls of the diffusion layer for symmetry reasons, and equilibrium for the hydrolysis of cations next to the Cu surfaces to account for this effect relevant at the atomic scale (see the Supplemental Experimental Procedures for calculation of the associated pKa). Critically, experimental partial current densities enabled to impose the flux of OH^- and CO_2 as the boundary condition on the Cu surfaces. In more detail, we considered

 CellPress

Chem
Article

the CO_2 consumption rate as linearly related to its concentration and the HER activity to increase linearly along the z axis (in line with reports claiming increased HER with decreasing local CO concentration[55]) by adapting the procedure developed by Raciti et al.[24] The reaction rate constants for both the HER and eCO_2RR were determined after imposing the matching of the measured current density corrected by the double-layer capacitance (Table S1) and the current density obtained after integrating the assumed reaction rates over the Cu surfaces (see the Supplemental Experimental Procedures for an extended description). The catalytic behavior of the ablated but non-microstructured surface (i.e., that between micro-probes) was considered equal to that of Cu-LA-0 (see Figure 2). The fragmented mechanistic information available led us to consider the reaction rates of all products to vary in the same manner along the z coordinate, which may not accurately reflect reality. This fact constitutes an opportunity for refinement in the future.

The populated set of results with 3D character and the complexity of the modeled volume demanded a strategy enabling a straightforward analysis. In view of the geometry of the micro-probes, we investigated whether the concentrations could be treated as one-dimensional (1D) without loss of generality. In fact, Figure S11 demonstrates that pH and CO_2 concentration can be accurately described as unidimensional variables solely dependent on the z coordinate in the interior of the micro-probes. In addition, the negligible mutual influence between adjacent probes was also unveiled. On a lateral note, a detailed analysis of the modeled flux of species revealed that L and potential can be used as descriptors of the CO_2 flux, exposing the interplay among geometry, potential, and mass transport (see Figures S12–S14).

Finally, we sought to quantify local concentrations of protons and CO_2 for each combination of potential and L. Figures 4B–4E show representative cases at low (−0.6 V) and high (−1.3 V) potentials for short (LA-Cu-40) and long (LA-Cu-100) microprobes. The combination of low potential and short length (Figure 4B) led not only to negligible depletion of CO_2 along the axis but also to a significant pH increase of more than one unit over the bulk at z = L. The application of low potentials to longer micro-probes (Figure 4D) did not have a strong impact on the concentration of CO_2 either, showing the ability of the buffered electrolyte and short diffusion paths to keep a homogeneous concentration at modest current densities (Table S4). However, the effect on the pH was even more noticeable. In the case of high potentials, short micro-probes (Figure 4C) also exhibited relatively high concentrations of CO_2 with the expected variation of pH. In contrast, long micro-probes (Figure 4E) developed large gradients of CO_2 concentration and pH along the axis (pH ∼ 10.2, $[CO_2]$ = 12 mol m^{-3} at z = 100 μm), suggesting a wide range of chemical environments at work. We can thus conclude that at low potentials, L can be used to tune the local pH while keeping a high and approximately constant CO_2 concentration throughout the volume, whereas at high potentials this strategy fails for large L values.

After these results, the pH and CO_2 concentration averaged over the z axis were taken as representative descriptors for further analyses. Maps relating these variables with L and potential are shown in Figure S15. A quick inspection reveals that the average CO_2 concentration is high and approximately constant in all experiments except for the combination of large L values and high potentials, whereas the average pH is mostly dependent on the applied potential and shows a wide plateau at pH 9–9.3 between −0.8 and −1.2 V versus RHE.

Chem
Article

CellPress

Figure 5. Selectivity Maps for eCO$_2$RR Products versus Chemical Environment Descriptors
Contour maps showing FE versus calculated average pH and CO$_2$ concentration in the interior of micro-probes. White regions correspond to pH/[CO$_2$] pairs not allowed by equilibria under reaction conditions.

Mapping Selectivity versus Chemical Environment Descriptors

As soon as potential and micro-probe length could be correlated to average pH and CO$_2$ concentration, we mapped selectivity values against them to expose patterns for each of the main products (Figure 5). As targeted, these maps are independent of the particular experimental setup used and thus reflect intrinsic trends of eCO$_2$RR on Cu materials. To confirm the kinetic nature of the maps, we mapped the current density associated to the formation of carbon products in Figure S16. From the lack of plateau regions, it can be inferred that mass transport limitations do not play a relevant role, and thus the observed patterns can be largely ascribed to mechanistic differences. In agreement with the lack of limiting current densities, average CO$_2$ concentrations were in all cases larger than 65% of the bulk value (34 mol m^{-3}; Table S9). At this point, we highlight the relevance of the local buffer effect of the hydrolysis of cations for an accurate assessment of the local chemical environment. The model proposed by Singh et al.[12] and incorporated into our calculations introduces a local source of protons through a fast hydrolysis equilibrium with a pKa of up to ~8 under high overpotentials (see the Supplemental Experimental Procedures). Figure S17 compares maps shown in Figure 5 with the equivalent maps where this effect is disregarded. Hydrolysis plays a modest role at mild conditions but becomes a large driver of the chemical environment at high overpotentials.

We now aim to provide a general perspective for all products by overlaying regions showing high selectivity. The resulting map after mathematical smoothing is displayed in Figure 6 (see Figure S18 for the unprocessed version including experiments modeled). Some relations among products become explicit on this representation, such as the intermediate position of the C$_3$ region between C$_1$ and C$_2$ at mild pH and high concentration of CO$_2$, where C$_2$ formations begin to rise but C$_1$ is still
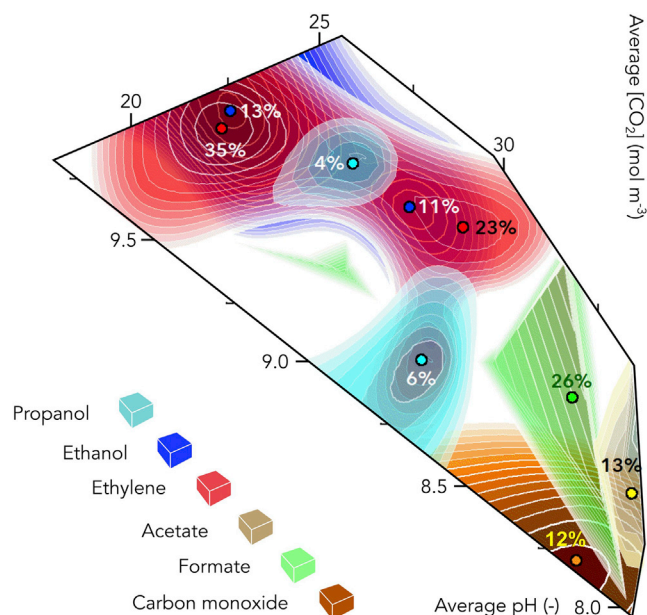
Figure 6. Combined Selectivity Map
Contour map showing high FE zones with respect to calculated average pH and CO$_2$ concentration in the interior of micro-probes upon overlaying and smoothing of maps presented in Figure 6. The dots represent local FE maxima. The equivalent map built upon direct overlapping of maps and including the experiments modeled can be found in Figure S13.

produced with appreciable activity. This suggests that mild overpotentials and good mass transport conditions may favor C$_3$ formation. In this regard, a second region for propanol (FE = 4% in Figure 7) overlapping the corresponding region for ethylene was identified by the mathematical treatment, suggesting a second mechanism at higher pH values where ethylene may play the role of intermediate. Finally, the lack of correlation between acetate and ethanol discards an impact of chemical routes (Cannizzaro-type reactions) in the formation of the latter.[11]

Mechanistic Relevance of Selectivity Maps
With regard to mechanistic considerations for specific products in maps displayed in Figure 5, the formate map points to its preferential formation under a relatively wide range of chemical environments (pH 8.0–9.8 and [CO$_2$] > 20 mol m^{-3}), suggesting a poorly sensitive mechanism. Carbon monoxide seems to share affinity for high concentrations of CO$_2$ constrained to a less alkaline pH range (<9). This observation agrees with the promotion of formate over carbon monoxide as the pH increases.[25] In addition, carbon monoxide shows lower selectivity in regions where C$_2$ products develop appreciably, in line with its accepted role of key intermediate.

The ethylene map presents two regions that call for a discussion in light of the proposed mechanisms associated with high and low overpotentials.[18,56,57] The first region is delimited by a narrow range of overpotentials and high pH values and contains a maximum FE (FE = 35%, [CO$_2$] = 22 mol m^{-3}, pH 9.9; see Tables S3 and S9) for LA-Cu-20 exposed to −1.3 V. In principle, this region could be reasonably ascribed to one of the high-overpotential mechanisms with strong pH dependence proposed either on Cu(111) or Cu(100). However, the small amount of methane produced (FE = 3% at the maximum; Table S3) suggests additional route(s) to those proposed by the Koper[56] and Goddard[57] groups. Similarly, the route proposed by
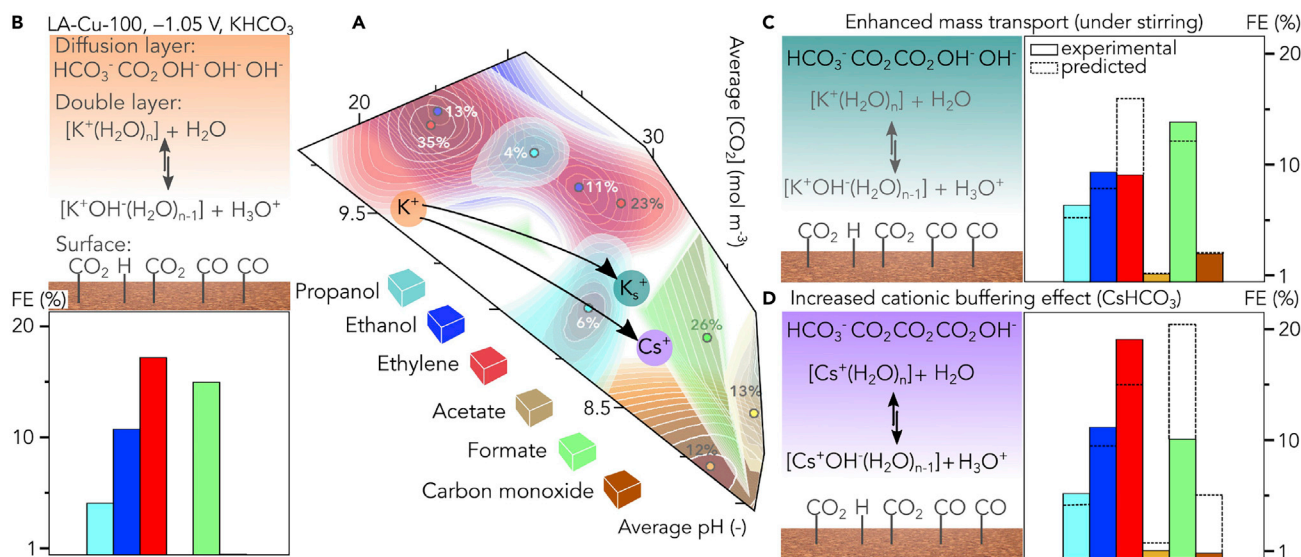
Figure 7. Effect of Enhanced Mass Transport and Electrolyte Composition on Selectivity

(A) A contour map from Figure 6 shows the calculated chemical environment for LA-Cu-100 exposed to -1.05 V versus RHE in 0.1 M KHCO$_3$ (K$^+$), 0.1 M KHCO$_3$ under stirring (K$_s^+$), and 0.1 M CsHCO$_3$ (Cs$^+$).

(B) Representation of the local chemical environment next to the surface and product distribution for the K$^+$ case.

(C and D) Similar to (B) but for the K$_s^+$ (C) and Cs$^+$ (D) cases with predicted selectivities obtained from maps in Figure 5 (dashed lines).

Head-Gordon et al.[58] is a problematic alternative in view of the small amount of acetate detected (FE $\sim$ 0.1%; Table S2). Interestingly, the other region with no distinct pH dependence at larger CO$_2$ concentrations (maximum at FE $\sim$ 30%, [CO$_2$] = 28 mol m^{-3}, pH 9.1, LA-Cu-130 operated at -0.8 V) might correspond to a low-overpotential route. Indeed, the relatively large amount of acetate (FE = 1%–3%) at the upper part of this region is compatible with some contribution arising from the Head-Gordon route.

The consideration of the ethanol pattern sheds additional light on this mechanistic discussion since it largely resembles that of ethylene (also observed in Figure 3). More specifically, the formation of ethylene glycol (FE $\sim$ 1%, [CO$_2$] =26 mM, pH 9.8) in the upper part of the region in association with larger CO$_2$ concentrations further supports the Head-Gordon pathway. However, this association cannot be extended to lower pH values, where the maximum FE for ethanol (overlapping the ethylene maximum) is located (FE = 9.8%, [CO$_2$] = 28 mol m^{-3}, pH 9.1). Regarding the other region, at higher pH values, both maxima also overlap (FE$_{ethanol}$ = 13.4%), and similarly, a tentative assignment of the predominant mechanistic route is precluded by the trace levels of the minor products quantified (Table S2). We thus conclude that despite the qualitative agreement, none of the proposed mechanistic routes for ethylene and/or ethanol closely match our observations, suggesting unaccounted pathways. Interestingly, the propanol map also discloses a discernible pattern.

Regrettably, the mechanistic discussion based on the literature is to date forcibly limited for C$_3$ products because of their yet largely unexplored reaction networks. Acetaldehyde has been recently proposed as a key intermediate toward propanol formation through its dehydrogenative adsorption as methyl carbonyl.[26] However, the very low FE observed for acetaldehyde in the region where the propanol FE peaks (<0.1%; Tables S2 and S3) makes it reasonable to assign a secondary relevance to this route in our study. Ethylene has also been proposed as a key

intermediate for the formation of propanol.[53,59,60] Our results reveal the high sensitivity of propanol formation to the chemical environment. At high CO_2 concentrations, it shows a nearly pH-independent optimal region that overlaps ethylene (maximum at FE = 5.4%, $[CO_2]$ =28 mol m^{-3}, pH 9.1), thus supporting their mechanistic relation. Given the dependency of eCO₂RR equilibrium potential on the concentration of protons and CO_2, we thus turned to investigate the overpotentials at which propanol was optimized. The overpotentials could be calculated from the Nernst equation upon correcting the standard reduction potential with the simulated concentration of species (Figure S9). The selectivity map in terms of local pH and overpotential (Figure S19) exhibits two favorable regions at mid (0.7 V) and high (1.1 V) overpotentials, suggesting that two mechanisms that have not been explored in the literature are at work.

Influence of Mass Transport and Electrolyte

In this section, we assess under which conditions and how selectivity maps may help define optimal operating conditions for selectivity control. Maps contribute to rationalize the largely reported sensitivity of eCO₂RR to the reactor configuration and operating conditions.

Cathodic catalysts in artificial leaves[1,61] usually operate in contact with liquid electrolyte and display <10 mA cm^{-2} current densities comparable to those reported in Table S4 as a result of the limited energy density of sunlight (ca. 1 kW m^{-2}). CO_2 electrolyzers fed by grid electricity, on the other hand, are typically designed on the basis of gas diffusion electrodes (GDEs), whose geometric current densities can reach hundreds of mA cm$_{geo}^{-2}$.[43] Nevertheless, the large electrochemical surface area typically reported over porous catalytic layers[62] of more than 30 m^2 g$_{metal}^{-1}$ leads to current densities of tens of mA cm$_{metal}^{-2}$ for typical catalyst loadings of 1 mg$_{metal}$ cm$_{geo}^{-2}$. Selectivity maps in Figure 5 are thus directly applicable to devices such as artificial leaves and can reasonably describe the main features of CO_2 electrolyzers operated below extreme current densities.

The transport of CO_2 to the active sites is typically enhanced either by the use of stirring in liquid medium or by the use of a GDE configuration. To understand the changes in the local chemical environment associated with enhanced mass transport, we exposed selected Cu-LA-L electrodes with very different geometries (L = 40,100) to potentials where mass transport expectedly plays a role (V = −1.05 and −1.3 V versus RHE) under mild stirring in 0.1 M KHCO₃. We computationally treated these experiments by considering 20 μm as the thickness of the diffusion layer (Figure 4A) after estimating it by using the Levich equation.[63] Local pH and CO_2 concentrations showed remarkable differences in comparison with the equivalent experiment without stirring (see Figure S20). Figure 7A displays the positions of representative examples (LA-Cu-100, −1.05 V versus RHE with and without stirring denoted as K$_s^+$ and K$^+$, respectively) in the global selectivity map. Stirring increased the average local CO_2 concentration from 22 to 29 mol cm^{-3} and concomitantly decreased the average pH from 9.6 to 9.2 (see Figures 7A and 7B; Table S9). Remarkably, the product distribution predicted for the stirring experiment by the position of K$_s^+$ in the map (dashed bars in Figure 7C) closely predicted the experimental distribution (solid bars). The large discrepancy found for ethylene could be related to the large gradients in its FE associated with that region (see Figure 5), making the predicted value very sensitive to small uncertainties in simulated results.

The electrolyte of choice in the eCO₂RR plays a critical role in both activity and selectivity, which has been linked to the local effect of the free cationic species

Chem
Article

CellPress

in the vicinity of the catalyst surface.[64] Larger cations are expected to show a lower pKa for their hydrolysis and a concomitant enlarged buffer capability (see the Supplemental Experimental Procedures for details on the calculations). We exposed Cu-LA-L electrodes (L = 0, 40, 100) to −1.05 V versus RHE in 0.1 M CsHCO$_3$ (no stirring applied) and simulated the local environment upon introducing Cs$^+$ hydrolysis equilibrium parameters to the model. Figure S20 illustrates how local pH and CO$_2$ concentrations varied notably along the axis of the microprobes with respect to the equivalent experiments in 0.1 M KHCO$_3$, facilitating a larger concentration of CO$_2$ and decreased pH. Figure 7A displays the position of the representative LA-Cu-100 exposed to −1.05 V versus RHE (denoted as Cs$^+$; Table S9). The use of CsHCO$_3$ allowed an increased CO$_2$ concentration (30 versus 22 mol cm^{-3}) and reduced pH (8.8 versus 9.6). Similarly to the case of K$_s^+$, the position of Cs$^+$ predicted with notable accuracy the experimental distribution of products (Figure 7C), with the exception of formate, for the same reasons explained for ethylene in the case of stirring. It is apparent from the comparison between K$_s^+$ and Cs$^+$ that enhanced mass transport and the electrolyte buffering effect play a somewhat similar role in varying the local chemical environment, though the latter is dependent on catalyst surface charge and thus on the potential.

From a more general perspective, these results reflect the ability of selectivity maps to account for the effect of operating conditions on the selectivity pattern. Given a target product, this feature could thus be used to orient basic design parameters. For example, the use of an electrolyte with mild cationic buffer effect such as KHCO$_3$ in combination with mild stirring seems an advisable combination for the selective production of propanol.

Conclusions

The application of microstructuring and advanced modeling enabled us to quantify the relation between selectivity and a broad range of chemical environments in the eCO$_2$RR on Cu. We unveiled selectivity maps for the main C$_1$–C$_3$ products in terms of local CO$_2$ concentration and pH by testing microstructured Cu foils processed by laser ablation and then performing simulations facilitated by the regular geometry of the electrodes. Selectivity maps disclosed clear patterns shedding light on open mechanistic queries. Ethylene and ethanol patterns could not be entirely accounted for by the proposed mechanisms, whereas the role of ethylene as an intermediate toward propanol is compatible with our results suggesting the presence of two mechanisms at mid and high overpotentials. From an operational perspective, selectivity maps successfully predicted the influence of operating conditions such as stirring or the use of different electrolyte on the product distribution, suggesting their potential to guide process design.

EXPERIMENTAL PROCEDURES

Resource Availability
Lead Contact
Further information and requests for resources and reagents should be directed to and will be fulfilled by the Lead Contact, Javier Pérez-Ramírez (jpr@chem.ethz.ch).

Materials Availability
This study did not generate new unique reagents.

Data and Code Availability
The published article includes all datasets generated or analyzed during this study.

⌀ CellPress

Chem
Article

Microstructuring, Characterization, and Modeling

Cu foils (0.3 mm, 20 × 20 mm) were processed by USP laser ablation[34,35] to impose geometry and chemical composition. The modified Cu oxide electrode (2.25 cm^2) comprised ca. 92,000 conical micro-probes with different lengths (0, 20, 40, 60, 100, and 130 μm). Electrodes were tested in a two-compartment custom-made gastight flow-cell with a three-electrode configuration in 0.1 M KHCO$_3$ or 0.1 M CsHCO$_3$ under continuous CO$_2$ bubbling with and without stirring (pH 6.8). The selectivity for gas products was determined by GC (H$_2$, CO, CH$_4$, and C$_2$H$_4$) and by ^{1}H-NMR for liquid ones (HCOO$^-$, C$_2$H$_3$OO$^-$, C$_2$H$_5$OH, C$_3$H$_7$OH, CH$_3$OH, C$_2$H$_4$O, C$_2$H$_6$O$_2$, and C$_3$H$_6$O). The morphology of catalytic surfaces was assessed by SEM, optical microscopy, microcomputed tomography and plasma-focused ion-beam SEM (PFIB-SEM), whereas the chemical composition was determined by XRD and XPS. All simulations were accomplished by a 3D finite-element method incorporating a MUMPS type solver in the COMSOL platform. Full details can be found in the Supplemental Experimental Procedures.

SUPPLEMENTAL INFORMATION

Supplemental Information can be found online at https://doi.org/10.1016/j.chempr.2020.04.001.

AUTHOR CONTRIBUTIONS

Conceptualization, A.J.M. and J.P.R.; Methodology, F.L.P.V. and A.J.M.; Formal Analysis, F.L.P.V. and A.J.M.; Investigation, F.L.P.V.; Resources, N.A.; Writing – Original Draft, F.L.P.V., N.A., and A.J.M.; Writing – Review & Editing, F.L.P.V., A.J.M., and J.P.R.; Visualization, F.L.P.V. and A.J.M.; Supervision, J.P.R.; Project Administration, F.L.P.V.; Funding Acquisition, J.P.R.

DECLARATION OF INTERESTS

The authors declare no competing interests.

REFERENCES

1. Martín, A.J., and Pérez-Ramírez, J. (2019). Heading to distributed electrocatalytic conversion of small abundant molecules into fuels, chemicals, and fertilizers. Joule 3, 2602–2621.

2. Kuhl, K.P., Cave, E.R., Abram, D.N., and Jaramillo, T.F. (2012). New insights into the electrochemical reduction of carbon dioxide on metallic copper surfaces. Energy Environ. Sci. 5, 7050–7059.

3. Nitopi, S., Bertheussen, E., Scott, S.B., Liu, X., Engstfeld, A.K., Horch, S., Seger, B., Stephens, I.E.L., Chan, K., Hahn, C., et al. (2019). Progress and perspectives of electrochemical CO₂ reduction on copper in aqueous electrolyte. Chem. Rev. 119, 7610–7672.

4. Birdja, Y.Y., Pérez-Gallent, E., Figueiredo, M.C., Göttle, A.J., Calle-Vallejo, F., and Koper, M.T.M. (2019). Advances and challenges in understanding the electrocatalytic conversion of carbon dioxide to fuels. Nat. Energy 4, 732–745.

5. Larrazábal, G.O., Martín, A.J., and Pérez-Ramírez, J. (2017). Building blocks for high

Chem
Article

CellPress

performance in electrocatalytic CO_2 reduction: materials, optimization strategies, and device engineering. J. Phys. Chem. Lett. 8, 3933–3944.

6. Vasileff, A., Xu, C., Jiao, Y., Zheng, Y., and Qiao, S.Z. (2018). Surface and interface engineering in copper-based bimetallic materials for selective CO_2 electroreduction. Chem 4, 1809–1831.

7. Zhang, L., Zhao, Z.J., and Gong, J. (2017). Nanostructured materials for heterogeneous electrocatalytic CO_2 reduction and their related reaction mechanisms. Angew. Chem. Int. Ed. 56, 11326–11353.

8. Liu, M., Pang, Y., Zhang, B., De Luna, P., Voznyy, O., Xu, J., Zheng, X., Dinh, C.T., Fan, F., Cao, C., et al. (2016). Enhanced electrocatalytic CO_2 reduction via field-induced reagent concentration. Nature 537, 382–386.

9. Dinh, C.T., Burdyny, T., Kibria, M.G., Seifitokaldani, A., Gabardo, C.M., García de Arquer, F.P., Kiani, A., Edwards, J.P., De Luna, P., Bushuyev, O.S., et al. (2018). CO_2 electroreduction to ethylene via hydroxide-mediated copper catalysis at an abrupt interface. Science 360, 783–787.

10. Varela, A.S., Kroschel, M., Reier, T., and Strasser, P. (2016). Controlling the selectivity of CO_2 electroreduction on copper: the effect of the electrolyte concentration and the importance of the local pH. Catal. Today 260, 8–13.

11. Birdja, Y.Y., and Koper, M.T.M. (2017). The importance of Cannizzaro-type reactions during electrocatalytic reduction of carbon dioxide. J. Am. Chem. Soc. 139, 2030–2034.

12. Singh, M.R., Kwon, Y., Lum, Y., Ager, J.W., and Bell, A.T. (2016). Hydrolysis of electrolyte cations enhances the electrochemical reduction of CO_2 over Ag and Cu. J. Am. Chem. Soc. 138, 13006–13012.

13. Chen, C.S., Wan, J.H., and Yeo, B.S. (2015). Electrochemical reduction of carbon dioxide to ethane using nanostructured Cu_2O-derived copper catalyst and palladium(II) chloride. J. Phys. Chem. C 119, 26875–26882.

14. Kas, R., Kortlever, R., Yılmaz, H., Koper, M.T.M., and Mul, G. (2015). Manipulating the hydrocarbon selectivity of copper nanoparticles in CO_2 electroreduction by process conditions. ChemElectroChem 2, 354–358.

15. Hori, Y., Murata, A., and Takahashi, R. (1989). Formation of hydrocarbons in the electrochemical reduction of carbon dioxide at a copper electrode in aqueous solution. J. Chem. Soc. Faraday Trans. 1 85, 2309–2326.

16. Raciti, D., Mao, M., Park, J.H., and Wang, C. (2018). Local pH effect in the CO_2 reduction reaction on high-surface-area copper electrocatalysts. J. Electrochem. Soc. 165, F799–F804.

17. Calle-Vallejo, F., and Koper, M.T.M. (2013). Theoretical considerations on the electroreduction of CO to C_2 Species on Cu(100) electrodes. Angew. Chem. Int. Ed. 52, 7282–7285.

18. Luo, W., Nie, X., Janik, M.J., and Asthagiri, A. (2016). Facet dependence of CO_2 reduction paths on Cu electrodes. ACS Catal. 6, 219–229.

19. Liu, X., Schlexer, P., Xiao, J., Ji, Y., Wang, L., Sandberg, R.B., Tang, M., Brown, K.S., Peng, H., Ringe, S., et al. (2019). pH effects on the electrochemical reduction of $CO_{(2)}$ towards C_2 products on stepped copper. Nat. Commun. 10, 32.

20. Hahn, C., Hatsukade, T., Kim, Y.G., Vailionis, A., Baricuatro, J.H., Higgins, D.C., Nitopi, S.A., Soriaga, M.P., and Jaramillo, T.F. (2017). Engineering Cu surfaces for the electrocatalytic conversion of CO_2: controlling selectivity toward oxygenates and hydrocarbons. Proc. Natl. Acad. Sci. USA 114, 5918–5923.

21. Kwon, Y., Lum, Y., Clark, E.L., Ager, J.W., and Bell, A.T. (2016). CO_2 electroreduction with enhanced ethylene and ethanol selectivity by nanostructuring polycrystalline copper. ChemElectroChem 3, 1012–1019.

22. Lim, C.F.C., Harrington, D.A., and Marshall, A.T. (2017). Effects of mass transfer on the electrocatalytic CO_2 reduction on Cu. Electrochim. Acta 238, 56–63.

23. Fuladpanjeh-Hojaghan, B., Elsutohy, M.M., Kabanov, V., Heyne, B., Trifkovic, M., and Roberts, E.P.L. (2019). In-operando mapping of pH distribution in electrochemical processes. Angew. Chem. Int. Ed. 58, 16815–16819.

24. Raciti, D., Mao, M., and Wang, C. (2018). Mass transport modelling for the electroreduction of CO_2 on Cu nanowires. Nanotechnology 29, 044001.

25. Bumroongsakulsawat, P., and Kelsall, G.H. (2014). Effect of solution pH on CO: formate formation rates during electrochemical reduction of aqueous CO_2 at Sn cathodes. Electrochim. Acta 141, 216–225.

26. Chang, X., Malkani, A., Yang, X., and Xu, B. (2020). Mechanistic insights into electroreductive C-C coupling between CO and acetaldehyde into multicarbon products. J. Am. Chem. Soc. 142, 2975–2983.

27. Rahaman, M., Dutta, A., Zanetti, A., and Broekmann, P. (2017). Electrochemical reduction of CO_2 into multicarbon alcohols on activated Cu mesh catalysts: an identical location (IL) study. ACS Catal. 7, 7946–7956.

28. Dutta, A., Rahaman, M., Mohos, M., Zanetti, A., and Broekmann, P. (2017). Electrochemical CO_2 conversion using skeleton (sponge) type of Cu catalysts. ACS Catal. 7, 5431–5437.

29. Song, H., Im, M., Song, J.T., Lim, J.-A., Kim, B.-S., Kwon, Y., Ryu, S., and Oh, J. (2018). Effect of mass transfer and kinetics in ordered Cu-mesostructures for electrochemical CO_2 reduction. Appl. Catal. B 232, 391–396.

30. Yang, K.D., Ko, W.R., Lee, J.H., Kim, S.J., Lee, H., Lee, M.H., and Nam, K.T. (2017). Morphology-directed selective production of ethylene or ethane from CO_2 on a Cu mesopore electrode. Angew. Chem. Int. Ed. 56, 796–800.

31. Larrazábal, G.O., Shinagawa, T., Martín, A.J., and Pérez-Ramírez, J. (2018). Microfabricated electrodes unravel the role of interfaces in multicomponent copper-based CO_2 reduction catalysts. Nat. Commun. 9, 1477.

32. Veenstra, F.L.P., Martín, A.J., and Pérez-Ramírez, J. (2019). Nitride-derived copper modified with indium as a selective and highly stable catalyst for the electroreduction of carbon dioxide. ChemSusChem 12, 3501–3508.

33. Lum, Y., and Ager, J.W., III. (2018). Sequential catalysis controls selectivity in electrochemical CO_2 reduction on Cu. Energy Environ. Sci. 11, 2935–2944.

34. Ackerl, N., Warhanek, M., Gysel, J., and Wegener, K. (2019). Ultrashort-pulsed laser machining of dental ceramic implants. J. Eur. Ceram. Soc. 39, 1635–1641.

35. Ackerl, N., Boerner, P., and Wegener, K. (2019). Toward application of hierarchical structures by ultrashort pulsed laser ablation. J. Laser Appl. 31, 022501.

36. Fang, H., Yang, J., Wen, M., and Wu, Q. (2018). Nanoalloy materials for chemical catalysis. Adv. Mater. 30, e1705698.

37. Lange, K., Schulz-Ruhtenberg, M., and Caro, J. (2017). Platinum electrodes for oxygen reduction catalysis designed by ultrashort pulse laser structuring. ChemElectroChem 4, 570–576.

38. Weber, R., Graf, T., Freitag, C., Feuer, A., Kononenko, T., and Konov, V.I. (2017). Processing constraints resulting from heat accumulation during pulsed and repetitive laser materials processing. Opt. Express 25, 3966–3979.

39. Lang, V., Roch, T., and Lasagni, A.F. (2016). High-speed surface structuring of polycarbonate using direct laser interference patterning: toward 1 m^2 min^{-1} fabrication speed barrier. Adv. Eng. Mater. 18, 1342–1348.

40. Chong, T.C., Hong, M.H., and Shi, L.P. (2010). Laser precision engineering: From microfabrication to nanoprocessing. Laser Photon. Rev. 4, 123–143.

41. Gillner, A., Finger, J., Gretzki, P., Niessen, M., Bartels, T., and Reininghaus, M. (2019). High power laser processing with ultrafast and multi-parallel beams. J. Laser Micro Nanoeng. 14, 129–137.

42. Nijhuis, T.A., Kreutzer, M.T., Romijn, A.C.J., Kapteijn, F., and Moulijn, J.A. (2001). Monolithic catalysts as efficient three-phase reactors. Chem. Eng. Sci. 56, 823–829.

43. Sánchez, O.G., Birdja, Y.Y., Bulut, M., Vaes, J., Breugelmans, T., and Pant, D. (2019). Recent advances in industrial CO_2 electroreduction. Curr. Opin. Green Sustain. Chem. 16, 47–56.

44. Raciti, D., Livi, K.J., and Wang, C. (2015). Highly dense Cu nanowires for low-overpotential CO_2 reduction. Nano Lett. 15, 6829–6835.

45. Min, S., Yang, X., Lu, A.-Y., Tseng, C.-C., Hedhili, M.N., Li, L.-J., and Huang, K.-W. (2016). Low overpotential and high current CO_2 reduction with surface reconstructed Cu foam electrodes. Nano Energy 27, 121–129.

46. Mariano, R.G., McKelvey, K., White, H.S., and Kanan, M.W. (2017). Selective increase in CO_2 electroreduction activity at grain-boundary surface terminations. Science 358, 1187–1192.

47. Feng, X., Jiang, K., Fan, S., and Kanan, M.W. (2015). Grain-boundary-dependent CO_2 electroreduction activity. J. Am. Chem. Soc. 137, 4606–4609.

⌬ CellPress

Chem
Article

48. Mistry, H., Varela, A.S., Bonifacio, C.S., Zegkinoglou, I., Sinev, I., Choi, Y.W., Kisslinger, K., Stach, E.A., Yang, J.C., Strasser, P., and Cuenya, B.R. (2016). Highly selective plasma-activated copper catalysts for carbon dioxide reduction to ethylene. Nat. Commun. 7, 12123.

49. Verdaguer-Casadevall, A., Li, C.W., Johansson, T.P., Scott, S.B., McKeown, J.T., Kumar, M., Stephens, I.E.L., Kanan, M.W., and Chorkendorff, I. (2015). Probing the active surface sites for CO reduction on oxide-derived copper electrocatalysts. J. Am. Chem. Soc. 137, 9808–9811.

50. Ren, D., Fong, J., and Yeo, B.S. (2018). The effects of currents and potentials on the selectivities of copper toward carbon dioxide electroreduction. Nat. Commun. 9, 925.

51. Hori, Y., Kikuchi, K., and Suzuki, S. (1985). Production of CO and CH_4 in electrochemical reduction of CO_2 at metal electrodes in aqueous hydrogencarbonate solution. Chem. Lett. 14, 1695–1698.

52. Kortlever, R., Peters, I., Balemans, C., Kas, R., Kwon, Y., Mul, G., and Koper, M.T.M. (2016). Palladium–gold catalyst for the electrochemical reduction of CO_2 to C_1–C_5 hydrocarbons. Chem. Commun. 52, 10229–10232.

53. Ren, D., Wong, N.T., Handoko, A.D., Huang, Y., and Yeo, B.S. (2016). Mechanistic insights into the enhanced activity and stability of agglomerated Cu nanocrystals for the electrochemical reduction of carbon dioxide to n-propanol. J. Phys. Chem. Lett. 7, 20–24.

54. Gupta, N., Gattrell, M., and MacDougall, B. (2006). Calculation for the cathode surface concentrations in the electrochemical reduction of CO_2 in $KHCO_3$ solutions. J. Appl. Electrochem. 36, 161–172.

55. Ooka, H., Figueiredo, M.C., and Koper, M.T.M. (2017). Competition between hydrogen evolution and carbon dioxide reduction on copper electrodes in mildly acidic media. Langmuir 33, 9307–9313.

56. Schouten, K.J.P., Qin, Z., Pérez Gallent, E.P., and Koper, M.T.M. (2012). Two pathways for the formation of ethylene in CO reduction on single-crystal copper electrodes. J. Am. Chem. Soc. 134, 9864–9867.

57. Cheng, T., Xiao, H., and Goddard, W.A. (2017). Full atomistic reaction mechanism with kinetics for CO reduction on Cu(100) from ab initio molecular dynamics free-energy calculations at 298 K. Proc. Natl. Acad. Sci. USA 114, 1795–1800.

58. Garza, A.J., Bell, A.T., and Head-Gordon, M. (2018). Mechanism of CO_2 reduction at copper surfaces: pathways to C_2 products. ACS Catal. 8, 1490–1499.

59. Zhuang, T.-T., Pang, Y., Liang, Z.-Q., Wang, Z., Li, Y., Tan, C.-S., Li, J., Dinh, C.T., De Luna, P., Hsieh, P.-L., et al. (2018). Copper nanocavities confine intermediates for efficient electrosynthesis of C_3 alcohol fuels from carbon monoxide. Nat. Catal. 1, 946–951.

60. Hori, Y., Takahashi, R., Yoshinami, Y., and Murata, A. (1997). Electrochemical reduction of CO at a copper electrode. J. Phys. Chem. B 101, 7075–7081.

61. Galan-Mascaros, J.R. (2020). Photoelectrochemical solar fuels from carbon dioxide, water and sunlight. Catal. Sci. Technol. 10, 1967–1974.

62. Brightman, E., Hinds, G., and O'Malley, R. (2013). In situ measurement of active catalyst surface area in fuel cell stacks. J. Power Sources 242, 244–254.

63. Bard, A.J., and Faulkner, L.R. (2012). Electrochemical Methods - Fundamentals and Applications (John Wiley & Sons, Inc).

64. Thorson, M.R., Siil, K.I., and Kenis, P.J.A. (2013). Effect of cations on the electrochemical conversion of CO_2 to CO. J. Electrochem. Soc. 160, F69–F74.